https://doi.org/10.1016/j.conbuildmat.2023.132110

Influence of seawater concentration on alkali-silica reaction of seawater sea-sand concrete: mimicking through NaCl solution and recycled glass aggregate

Yangyang Zhang [a,d], *Qunli Zhang* [a,d], *Caihong Xue* [a,d], *Kai Wu* [c], *Jun Chang* [e], *Jianxin Lu* [b], *Peiliang Shen* [b], *Qingxin Zhao* [a,d,*], *Chi Sun Poon* [b,*]

[a] State Key Laboratory of Metastable Materials Science and Technology, Yanshan University, Qinhuangdao, 066004, China

[b] Department of Civil and Environmental Engineering, The Hong Kong Polytechnic University, Hung Hom, Kowloon, Hong Kong, China

[c] Key Laboratory of Advanced Civil Engineering Materials of Ministry of Education, School of Materials Science and Engineering, Tongji University, Shanghai 201804, China

[d] Hebei Province Engineering Research Center for Harmless Synergistic Treatment and Recycling of Municipal Solid Waste, Yanshan University, Qinhuangdao, 066004, China

[e] School of Civil Engineering, Dalian University of Technology, Dalian 116024, Liaoning, China

*Corresponding author

E-mail: zhaoqx2002@163.com (Qingxin Zhao)

cecspoon@polyu.edu.hk (Chi Sun Poon)

Abstract

Seawater sea-sand concrete (SSC) is one environment-friendly and promising construction material. Nevertheless, limited research shed favorable light on alkali-silica reaction (ASR) of SSC. This work provided a novel insight regarding the fast test method that (i) the recycled glass aggregate (RGA) was used for fast assessing the effect of seawater concentration on ASR, reusing its characteristic resource; (ii) the NaCl solutions with different concentrations were used to mimic different salinities of sea waters; and (iii) a modified curing method was adopted. The results showed that the NaCl solution could be used for assessing ASR risk of SSC instead of seawater. The specimens mixed with twice and above the sodium concentration of seawater would exhibit ASR expansion, strength reduction, coarsening of nanopore distribution, and the cracks on the macro and micro levels. However, the change of NaCl concentration scarcely affected the composition and content of hydration products. Additionally, with increasing the mixing Na^+ concentration, the ASR crack would firstly appear in the interface between the cement paste layer and the glass layer, and then developed in the internal zone of RGA matrix with different hardness, elastic modulus, and Si contents based on the destroyed degree.

Key words: Recycled glass aggregate; Seawater sea-sand concrete; Alkali-silica reaction; Nanoindentation; Microstructure

1. Introduction

The concrete production consumes 16.6×10^9 m^3 of freshwater per year, accounting for about 18% of industrial freshwater consumption across the world annually [1]. Some estimates suggest

that the concrete production would experience 75% of the water demand in regions where the freshwater stress is expected to occur [1], and over 50% population worldwide is likely to suffer from freshwater shortage for daily life by 2050 [2], especially for the regions (e.g., North Africa, Middle East or some outlying islands) that have had difficulties accessing sufficient freshwater [3, 4]. Besides freshwater, the concrete production also experiences the shortage of river sand since its overexploitation is threatening river ecosystems, navigation and flood control [5].

Seawater sea-sand concrete (SSC), manufactured by utilizing seawater as an alternative to freshwater and sea-sand as an alternative to river sand, is seeing increasing interest worldwide based on the evidences including (i) some large funded proposals, (ii) numerous research papers regarding SSC annually, (iii) six review papers published regarding SSC recently, (iv) a related special issue published by Advances in Civil Engineering Materials, (v) some SSC based infrastructures that are already applied (e.g., the Great Belt Bridge and the Olympic Stadium in London), and etc. [5-11]. Furthermore, considering the potential steel corrosion owing to the presence of chloride in seawater or sea-sand, SSC could be applied in plain concrete, conventional steel reinforced concrete with corrosion inhibitors, and fiber reinforced polymer (FRP) reinforced concrete [12-17].

Much of research have given priority to investigating the mechanical strength and hydration mechanism of SSC. Regarding the mechanical strength of SSC, most findings reveal that the usage of seawater or sea-sand could increase the early-age strength since the active ions of seawater accelerate the hydration of cement pastes [5, 6, 18-20], but slightly degrade the long-term

compressive strength [18, 21-24] owing to (i) the leaching of hydration products [24], (ii) the salt crystallization and expansion of brucite and gypsum [25], (iii) a shorter silica chain of C-S-H [18], and (iv) the deleterious effect of Mg^{2+} in seawater [4]. As for the hydration mechanism of SSC, some hot research areas are increasingly comprehensible, including (i) the reasons for acceleration effect of seawater [20, 26-28], (ii) the track of Cl^- ion in seawater (e.g., the formation of Friedel's salt or calcium oxychloride compounds with a chemical composition of $xCa(OH)_2 \cdot yCaCl_2 \cdot zH_2O$, the absorption of C-S-H, and etc.) [8, 27, 28], (iii) the change of C-S-H (e.g., its composition, morphology, micro-mechanical property, and etc.) [4, 18, 20, 26, 29], (iv) the effect of other ions (SO_4^{2-}, CO_3^{2-}, Na^+, Ca^{2+} and Mg^{2+}) in seawater on hydration products and chloride binding [4, 8, 20, 30, 31], and etc.

However, there have been limited studies in extent that focused on the durability of SSC, restricting its widespread application. With regard to the durability, some researches have understood in extent the effect of seawater on shrinkage, where it is suggested that the usage of seawater would slightly increase the drying shrinkage at a lower water-to-cement (W/C) ratio, but this effect would become substantial with an increase of W/C, especially in the lightweight concrete [6, 8, 22, 32, 33]. Nevertheless, up to now, few studies shed enough light on alkali-silica reaction (ASR) of SSC. During the actual production of SSC, the reactive aggregate would be difficult to avoid non-existence entirely. Owing to the high alkali in seawater, it is indicated that the potential ASR degradation might occur in SSC with reactive aggregates, whilst the further research is needed [34-36].

Furthermore, seawater with varied salinities is present across the world although the average salinity of seawater is about 3.5%, e.g., Baltic Sea with the salinity of 1.0%, Red Sea with the salinity of 4.1%, Dead Sea with the salinity of 34.2%, Lagoon Garabogazköl in the Caspian Sea with the salinity of 35%, etc. Also, the salinity of seawater fluctuates with the seasons. Additionally, different water-to-cement ratios are used in civil engineering, corresponding to different salt contents. Besides, the construction would suffer from a very large salinity when applied in marine structures. Moreover, the usage of sea-sand also increases the whole salinity. Hence, the varied salinities would induce different degrees of ASR degradation during the service life of SSC due to the varied contents of alkali metals. However, there have been no studies that investigate the effect of seawater concentration on ASR of SSC.

This work provided a novel insight, i.e., using recycled glass aggregate (RGA) as the active aggregates for fast investigating the effect of seawater concentration on ASR, which reuses its characteristic resource. Additionally, this work took a page from the method of evaluating chloride ingress that used NaCl solution to perform the chloride ingress testing instead of seawater [37], i.e., this work investigated whether NaCl solution could be used for assessing the ASR risk of SSC instead of seawater in view of the complexity of seawater composition. Also, the NaCl solutions with different concentrations were prepared to mimic the effect of seawater concentration on ASR, corresponding to various marine conditions ranging from a common environment to an extreme environment, which contributed to designing the structures with high ASR resistance during their service life. Moreover, this work used a fast curing method by modifying ASTM C1260. In this work, the macro-performance and microstructure of the specimens mixed with NaCl solutions

were studied. Furthermore, the ASR crack process of RGA was investigated from a nanomechanical strength perspective.

2. Experimental program

2.1 Materials

In this work, Ordinary Portland cement (OPC, a specific gravity of 3.15) complying with ASTM Type I was used. The chemical compositions were obtained by X-ray fluorescence spectroscopy (Supermin200, Rangaku Corporation, Japan), as shown in Table 1. The values of D_{10}, D_{50} and D_{90} were 2.34 um, 14.45 um and 35.34 um, respectively. The clinker composition, calculating by Rietveld refinement, was 66.4 wt.% of C_3S, 11.9 wt.% of C_2S, 6.0 wt.% of C_3A, 7.2 wt.% of C_4AF, 5.8 wt.% of $CaCO_3$ and 2.7 wt.% of gypsum.

The recycled glass aggregate (RGA) with a size of 0.15-5 mm and river sand with a size of 0.15-5 mm were used as fine aggregates. The RGA, sourced from a waste glass recycling plant, had a high ASR reactivity owing to high-active SiO_2 content (Table 1). The river sand was a non-alkali reactive natural aggregate. The densities of RGA and river sand were 2.52 g/cm^3 and 2.60 g/cm^3, respectively. The waste glass cullet and river sand were washed and dried at 105 °C for 2 days. This work followed the same source of recycled glass cullet for consistency. The resulting RGA exhibited a fine modulus of 3.44.

Table 1 Chemical compositions of OPC and RGA (wt%)

Oxide	CaO	SiO_2	Al_2O_3	Na_2O	Fe_2O_3	SO_3	MgO	K_2O	Others
OPC	66.10	20.00	5.13	-	3.24	2.99	1.09	-	1.45
RGA	10.97	71.67	1.25	13.71	0.37	-	1.20	0.60	0.23

The artificial seawater with a salinity of 3.5% was prepared according to ASTM D1141-98 [38]. Considering different salinities concerning sea waters and the extreme condition concerning the corresponding environmental concrete exposure, various NaCl concentration solutions were prepared by mixing analytical grade NaCl with deionized water, i.e., N1 solution (the same sodium concentration as the seawater), N2 solution (twice the sodium concentration of seawater), N4 solution (four times the sodium concentration of seawater), N8 solution (eight times the sodium concentration of seawater). Table 2 lists the Na^+ concentration in different solutions.

Table 2 Na^+ concentration of different solutions (g/L)

	Deionized water	Seawater	N1	N2	N4	N8
Na^+ concentration	0	11.02	11.02	22.04	44.08	88.16

2.2 Specimen preparation

Different specimens were prepared according to the type of mixed water, i.e., D specimen (using deionized water), S specimen (using seawater), N1 specimen (using N1 solution), N2 specimen (using N2 solution), and N4 specimen (using N4 solution). The experimental method used in this work was chosen based on the following preliminary experiments.

The first method was used as follows: The mortar mixes were prepared according to ASTM C 1260. Both of RGA and river sand were used as fine aggregates with a ratio of 1:1. The specimens were prepared using an aggregate-to-cement ratio of 2.25 and a water-to-cement ratio of 0.47. The D, S, N1, N2 and N4 specimens were cast into 25 mm × 25 mm × 285 mm steel cube molds, and three specimens were prepared from each mix. And then the specimens were covered by polyethylene sheets and cured for 24 h. After demolding, the specimens were cured in water bath at 80 °C for 24 h, and then in 1 M NaOH solution at 80 °C for 3, 7, 14, 21 and 28 days, respectively. For each age, the specimens were subjected to length measurements, and the ASR expansion was determined by the average value of three specimens.

Secondly, a modified method was used. The mortar specimens were prepared using the same production process described above. After demolded, the specimens were only cured in deionized water bath at 80 °C for the same ages mentioned above.

The third method was proposed and used based on the second experimental method, i.e., (i) 100% RGA was used in the mixes as fine aggregates, and (ii) a higher NaCl concentration solution (i.e., N8 solution) was prepared as the mixing solution. The aggregate-to-cement ratio and the water-to-cement ratio were consistent with the experimental methods describe above. The well-mixed mortars were cast into 25 mm × 25 mm × 285 mm molds for expansion test and 40 mm × 40 mm × 40 mm molds for compressive strength test. After 24 h of curing in the molds, the specimens were demolded and transferred into the deionized water bath at 80 °C. The specimens were taken out to measure the expansion and compressive strength values after cured for 1, 3, 7,

14, 21 and 28 days. The 28-day specimens were broken into small particles, stirred in isopropanol for 5 minutes, and then vacuum dried for 1 day prior to the microstructure analysis [39, 40].

2.3 Characterization

2.3.1 Electrochemical impedance spectroscopy (EIS)

EIS measurement was carried out by a Multi-AutolabM 204 instrument equipped with a frequency ranging from 10 mHz to 1 MHz and an AC signal magnitude of 10 mV. For each 40 mm × 40 mm × 40 mm cubic specimen, two thin wet sponges were covered its surface for obtaining a favorable electrical contact. In this work, a two-electrode system was used for measuring the impedance modulus data, and Nova 1.11 software was used for analyzing the resulting impedance spectra.

2.3.2 Nitrogen adsorption and desorption (NAD)

NAD curves were recorded by an ASAP 2020 Micromeritics Accelerated Surface Area and Porosimetry instrument. The small particles were degassed at 60 °C and a pressure of 0.1 mmHg for 24 h, and then measured with a bath temperature of -196 °C. Barrett-Joyner-Halenda (BJH) analysis was conducted to obtain the pore volume distribution.

2.3.3 Heat hydration

The hydration heat of each cement paste specimen was conducted by a Calmetrix I-Cal 4000 isothermal calorimeter. The different pastes were prepared by mixing OPC with various NaCl concentration solutions for 2 min before the hydration heat test, and immediately measured for up to 3 d in the calorimeter.

2.3.4 X-ray diffraction (XRD)

XRD curves were acquired by a Bruker D8 Advance X-Ray Powder Diffractometer equipped with a LYNXEYE XE-T detector where the operation voltage was 40 kV and the operation current was 40 mA. The overall acquiring time of each curve was about 30 min at 5.0° to 80.0° 2θ with a step size of 0.020° and a rate of 0.5 s per step, ensuring a favorable signal-to-noise ratio. For Rietveld refinement, 10 wt% α-Al_2O_3 (Aladdin, 99.99% purity), as an internal standard, was well mixed with the hydrated powder, and TOPAS 4.2 software was used for calculating the content of crystalline and noncrystalline (Acn) phases. The Rietveld refinement parameters include background coefficients, phase scale factors, zero-shift error, Chebyshev polynomial correction, Lorentz polarization factor, cell parameters and crystal structures. Table 3 shows the corresponding ICSD codes of different minerals.

Table 3 Phase compositions and the corresponding ICSD codes.

Phase	ICSD Codes
C_3S	4331
C_2S	81096
C_3A	1841
C_4AF	9197
$C\check{S}H_2$	36186
$CaCO_3$	18165
CH	34241
AFt	155395
Friedel's salt	62363
Al_2O_3	10425

2.3.5 Backscattered electron (BSE) / energy dispersive spectroscopy (EDS)

BSE images were observed by a TESCAN VEGA3 instrument with an acceleration voltage of 20 kV and a working distance of 16 ± 0.5 mm. The specimen particles were firstly impregnated by an epoxy resin (EPO-TEK 301) under a vacuum pressure of 10 mbar where the air could be well

removed and the epoxy resin could be well infiltrated. After solidified for 24 h, the resulting specimens were ground and polished by a Buehler AutoMet 300 equipment, and the procedures in details were reported in the previous work [41] where isopropanol was used instead of water during the beginning steps. The well-polished samples were coated with carbon by a SPI Module™ Carbon Coater. Also, EDS elemental mapping was performed in the selected areas.

2.3.6 Nanoindentation

Nanoindentation measurements were carried out by a Hysitron Triboindenter 950 system (TI 950 TriboIndenter, Bruker) where a Berkovich diamond indenter probe was used. The sample preparation method was similar to the one used for BSE observations shown in Section 2.3.5. Prior to nanoindentation measurements, the surface roughness in the selected area was determined, satisfying the maximum of 70 nm threshold [42]. The peak load was set at 2000 μN, and a measurement procedure of loading time of 10 s, holding time of 5 s and unloading time of 10 s was adopted in this study. For each nanoindentation measurement, an interval of 5 μm was determined, but various grids were chosen for effectively detecting the nanoscale strength evolution in the ASR crack region. The hardness and elastic modulus of each nanoindentation were determined complying with the previous guidelines [43].

3. Results

3.1 ASR expansion

Fig. 1 shows the dimensional changes of different specimens prepared and subjected to expansion test according to the first method, i.e., based on ASTM C1260. It can be found that the expansion

values of all mortar specimens exceeded the 0.1% ASTM C1260 threshold. In addition, the expansion values of all specimens continually increased as the curing age prolonged. Thus, the first method was not suitable to evaluate the effect of different seawater concentrations on ASR since the Na^+ ions present in the external cured solution played a dominant role and the effect of Na^+ ions in the mixed water was extremely weak with respect to the ASR expansion of these specimens.

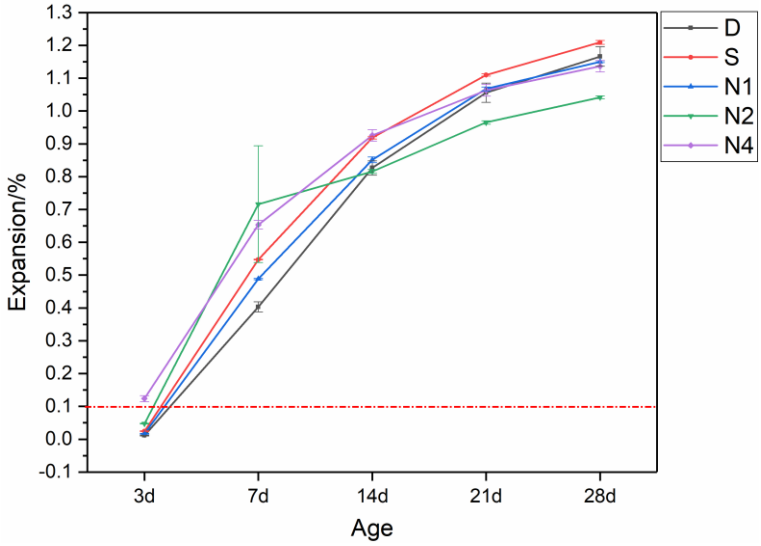

Fig. 1 Expansion of different mortar bar specimens with 50% RGA prepared based on ASTM C1260.

Fig. 2 shows the expansion values of different specimens prepared and subjected to expansion test according to the second method. It can be seen that the expansion value of each specimen was below the threshold value even prolonged the curing age up to 28 days, although the D4 specimen exhibited a higher expansion compared to other specimens with a lower NaCl concentration. Thus, this method was also not appropriate to fast evaluate the effect of various seawater salinities on ASR.

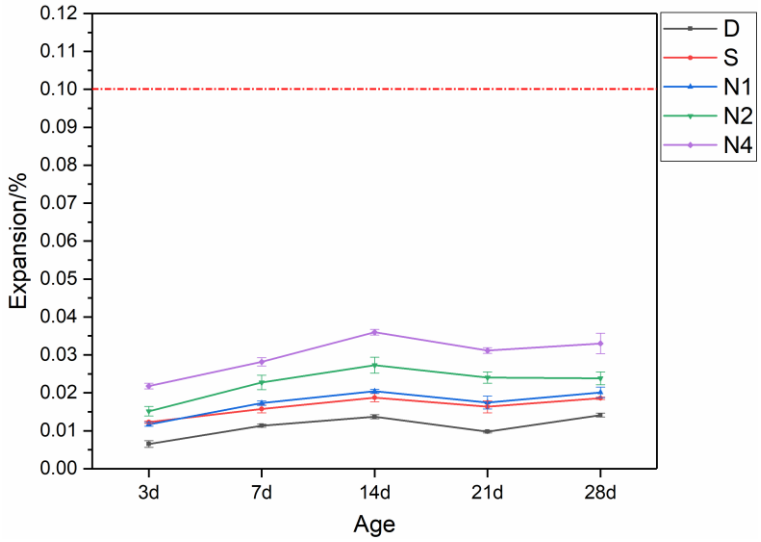

Fig. 2 Expansion of different mortar bar specimens with 50% RGA cured in 80 °C deionized water.

Fig. 3 shows the ASR expansion values of different specimens prepared and subjected to expansion test according to the third method, i.e., using 100% RGA and mixing various Na^+ ion concentrations ranging from one time to eight times the Na^+ concentration of seawater. The effect of various seawater concentrations on ASR can be seen. Firstly, the expansion values of all specimens were lower than the 0.1% ASTM C1260 threshold before 3 days of 80 °C water curing. However, the expansions of N4 and N8 specimens exceeded the threshold value at 7 days, and significantly increased with an increase of exposure ages. Regarding the specimen mixed with twice the Na^+ concentration of seawater, the expansion just met the 0.1% threshold at 14 days, but the ASR expansion was obviously observed at 21 and 28 days, respectively. The N1 specimen exhibited similar expansion values at each exposure age, compared with S sample, although the expansion values of S and N1 specimens were slightly higher than that of D specimen, which indicated that (i) ASR testing could be carried out using NaCl solution instead of seawater, and (ii) the seawater mixed specimen well met the ASTM C1260 threshold even prolonged the exposure

age up to 28 days. Moreover, an increase in ASR expansion was detected with increasing the mixed NaCl solution concentration, especially for that the ASR expansion dramatically increased with increasing NaCl solution concentration from 2 times to 4 times the sodium concentration of seawater. Thus, the third method was suitable, and the following tests and analysis were based on the specimens prepared by this method.

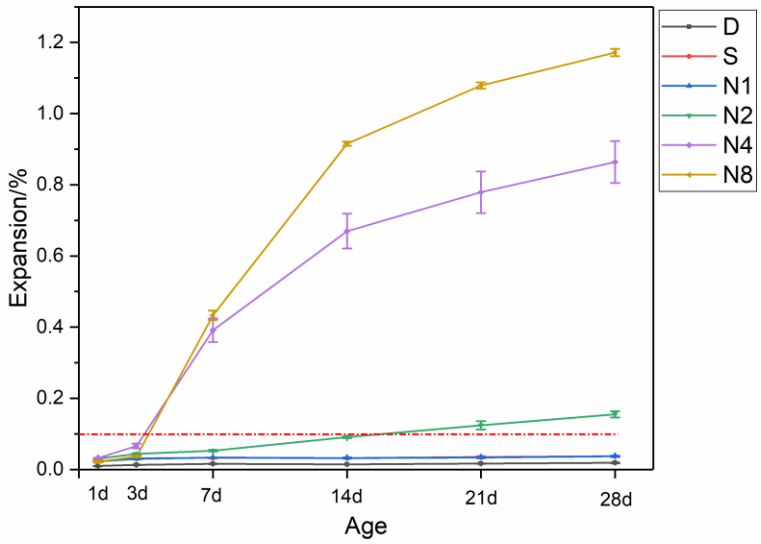

Fig. 3 Expansion of different mortar bar specimens with 100% RGA cured in 80 °C deionized water.

3.2 Mechanical strength

The compressive strength of the cubic specimens mixed with different Na^+ ion concentrations was also investigated, as shown in Fig. 4. The results show that compared with the reference specimen (D specimen), the seawater or NaCl solution mixed specimens exhibited a lower compressive strength after cured in water bath at 80 °C for different ages. However, the seawater mixed mortar specimen shows a slightly lower or similar compressive strength in comparison with the DI water mixed specimen. Also, a similar 28-day compressive strength is observed for the specimen mixed with seawater and the specimen mixed with the same sodium concentration of seawater, which is

consistent with the ASR expansion result (Fig. 3). Additionally, a decrease in the 28-day compressive strength was seen with the increase of the mixed NaCl solution from one time to eight times the sodium concentration of seawater.

It was also observed in Fig.4 that N2 specimen showed a significant decrease in compressive strength after 28 days compared to the 7-day compressive strength, although its compressive strength increasingly gained in the first 7 day of steam curing. However, regarding N4 and N8 specimen, this decrease phenomenon had taken place at 7 days, and severely deteriorated as the curing age prolonged. Therefore, the evolution of compressive strength of N2, N4 and N8 specimens well reflected the corresponding ASR expansion process, i.e., as shown in Figs. 3 and 4, the compressive strength was not negatively affected when the expansion values were below 0.1% threshold, however, the ASR gel would exert pressure and deteriorate the compressive strength as the expansions exceeded the threshold value of 1%, and cracking developed and further reduced the strength with an increase of expansion values.

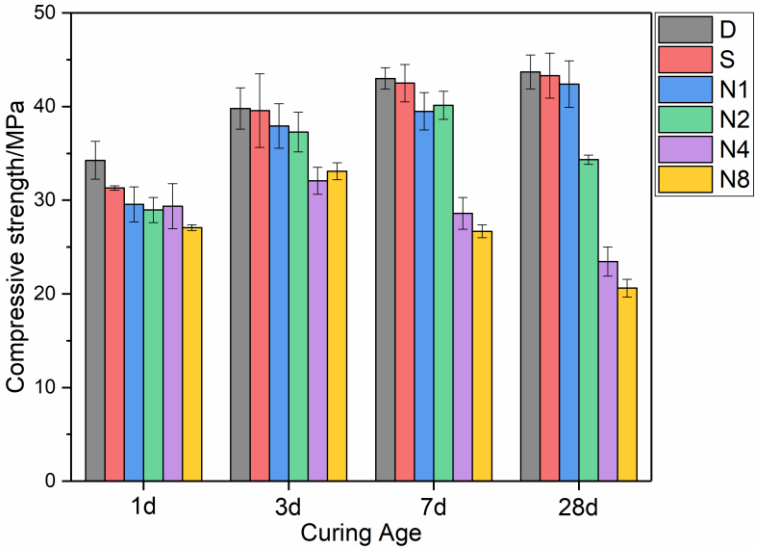

Fig. 4 Compressive strength of different cubic specimens at 1, 3, 7 and 28 days.

3.3 Evolution of macro crack

Generally, the swelling pressure of ASR gel would induce cracks. Fig. 5 shows the macro images of the surface of different specimens cured in water bath at 80 °C for 28 days, observed by an optical microscope. The crack width was measured, and about 50 images of the crack per specimen were recorded and analyzed by Image J software, as shown in Fig. 6.

It is observed in Fig. 5 that no cracks were detected in D, S and N1 specimens, indicating that ASR expansion was not present in these three specimens, which was also consistent with the expansion results in Fig. 3. However, the cracks with different widths were observed in N2, N4 and N8 specimens, and the crack width significantly increased with an increase in the mixed Na^+ concentration. Moreover, as the statistics shown in Fig. 6, N2 specimen showed a varied crack width from 20.3 um to 46.0 um with a mean of 33.8 um, N4 specimen exhibited a large crack width from 189.4 um to 372.0 um with a mean of 263.6 um, while N8 specimen presented an increasingly large crack width from 342.2 um to 652.4 um with a mean of 513.1 um. Therefore, the evolution of crack width with the change of mixed Na^+ concentration was quantified, and the crack developed severely with an increase of the mixed Na^+ concentration from 2 times to 4 times to 8 times the sodium concentration of seawater, corresponding to the significant increase in expansion values (Fig. 3) and decrease in compressive strength (Fig. 4).

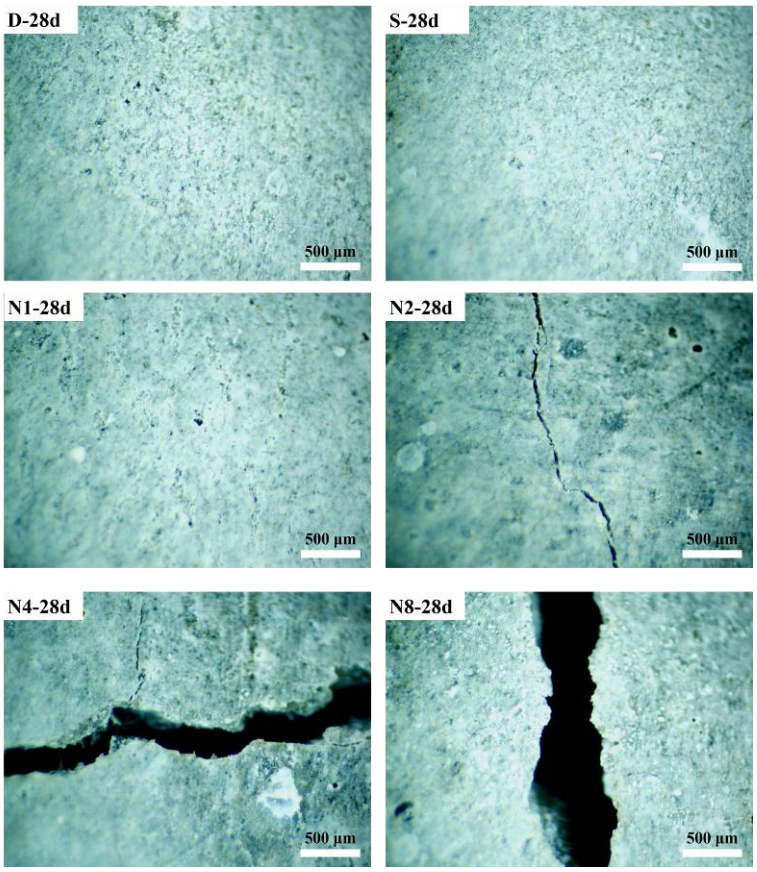

Fig. 5 Macro images of the surface of different specimens at 28 days

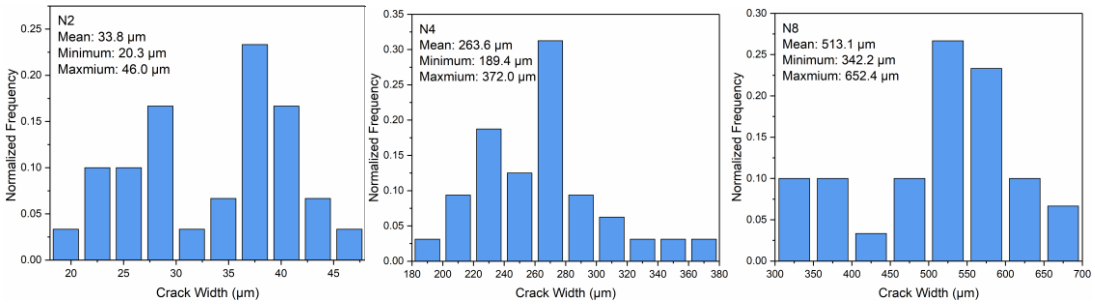

Fig. 6 Crack width distribution of N2, N4 and N8 specimens

3.4 Evolution of nanopore structure

The evolution of nanopore structure of the specimens mixed with different Na^+ concentrations was investigated by nitrogen adsorption and desorption method, as shown in Fig. 7. The results show that the absorption total pore volume changed with an increase of the mixed Na^+ concentration,

increasing from 0.077 cm^3/g (D specimen) to 0.097 cm^3/g (N4 specimen). The BJH adsorption average pore diameter increased from 13.24 nm (D specimen) to 15.84 nm (N8 specimen). Therefore, the mixing of Na^+ ion would also trigger the increase of total nanopore volume and nanopore diameter in addition to the evolution of macro crack (Fig. 6).

In order to clearly figure out the negative effect of mixing Na^+ ion concentration on the nanopore structure, the nanopore volume distribution of different mortar specimens was further investigated, as shown in Fig. 8. Generally, the pore size could be divided into the following size ranges [44, 45]: gel pores with pore diameters lower than 10 nm, mesopores with pore diameters ranging from 10 nm to 50 nm, medium capillary pores with pore diameters ranging from 50 nm to 100 nm, and large capillary pores with pore diameters over 100 nm. It can be observed in Fig. 8 that the nanopore volume distribution of mortar specimens changed after mixing Na^+ ion, i.e., the content of gel pores decreased and that of large capillary pores increased as the mixing Na^+ ion concentration increased, indicating that the pore structure was coarsened. Furthermore, after mixing Na^+ ion, the small gel pore with a diameter less than 3 nm obviously increased, the pore with the diameters ranging from 3 nm to 10 nm was low in content, but the pore volume increased starting from 20 nm of diameter, as shown in Fig. 7. Therefore, the nanopore distribution was coarsened in the NaCl mixed specimens, compared with the DI water mixed specimen.

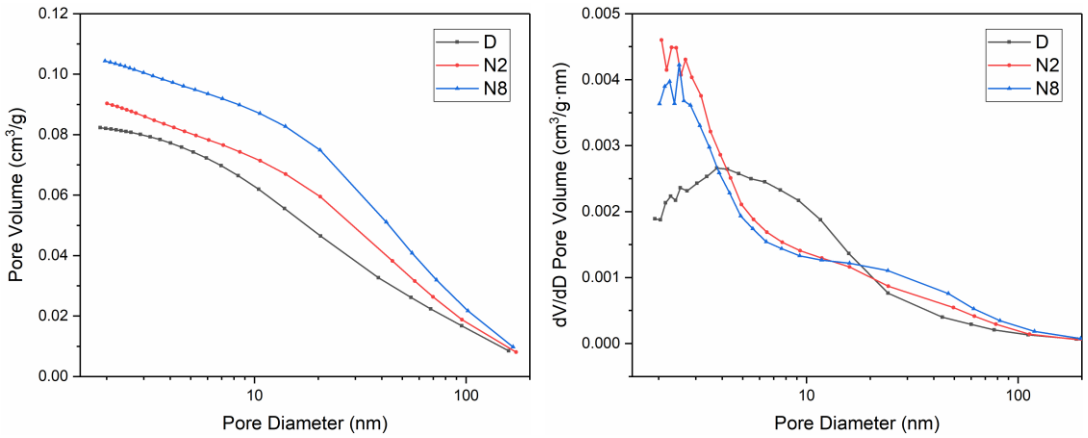

Fig. 7 BJH adsorption curves of different mortar specimens at 28 days.

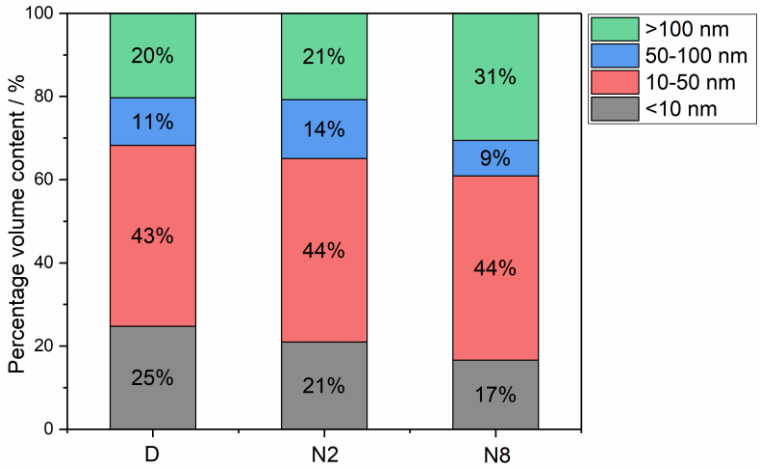

Fig. 8 Nanopore volume distribution of different mortar specimens at 28 days

3.5 Evolution of bulk electrical resistance

Fig. 9 shows the results of electrochemical impedance test of the cubic specimens mixed with different Na^+ ion concentrations, which was beneficial to understand the effect of mixing Na^+ ion concentration on external ions/water transportation rate. For each impedance spectrum, impedance modulus is the intersection abscissa of the bulk arc and electrode arc [46]. It can be seen that the impedance modulus at 1 day gradually decreased with increasing the mixing Na^+ ion concentration, indicating that the external water more easily transported and came into the

specimens as the higher Na^+ ion concentration was mixed. It is worth noting that the ASR expansion of all the specimens did not occur at 1 day (Fig. 3), and thus the mixing Na^+ ion (i) accelerated the external water transportation and (ii) provided the Na source of ASR at the early age. Therefore, the specimen mixed with a higher Na^+ ion concentration easily formed ASR gel, exhibiting higher swelling pressure and severer ASR cracks, as the exposure age prolonged (Fig. 3). In addition, the impedance modulus at the later age (i.e., 28 days shown in Fig. 9) also showed a similar evolution compared to 1 day, which was caused by the changes of crack width and mixing Na^+ ion concentration.

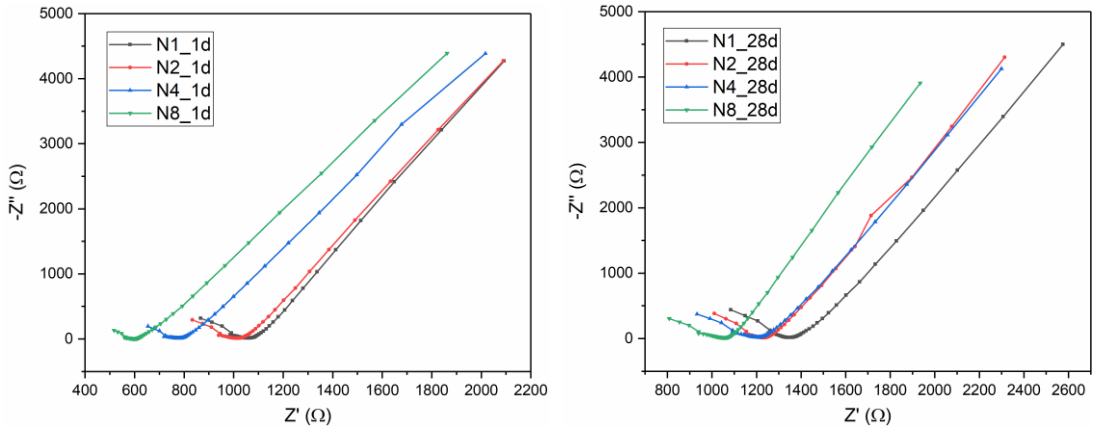

Fig. 9 EIS results of the specimens mixed with different sodium concentrations at 1 and 28 days

3.6 Effect of NaCl concentration on hydration

In this work, the effect of the mixing NaCl concentration on the hydration rate and products was also investigated. Fig. 10 shows the heat flow and cumulative heat curves of the cement pastes mixed with different NaCl concentrations. It can be seen from the heat flow curves that the peaks of heat flow in S, N1, N2 and N4 specimens appeared earlier (about 1.5 hours) and were also higher, compared with the reference sample (DI water mixed specimen). Therefore, the addition of

seawater or NaCl solution could accelerate the hydration rate, which was in line with other works [4, 6, 8, 47]. However, it is interesting to observe that the heat flow peak of N8 specimen shifted right and was lower compared to that of D specimen, corresponding to a relatively slower hydration rate presented in N8 specimen. Therefore, a very high NaCl concentration would delay the hydration rate of cement pastes. However, this delay only existed at the very early age, i.e., the heat flow of N8 specimen was higher than that of D specimen starting from 15 hours of hydration, as shown in Fig. 10. Additionally, the cumulative heat results clearly showed the effect of NaCl concentration on the hydration rate. It can be observed that the S, N1, N2 and N4 specimens released a high hydration heat at each hydration time, compared to D specimen. The cumulative heat value of N8 specimen was lower than that of D specimen before 21 hours of hydration, but increased significantly and exceeded that of D specimen afterward. Moreover, the specimens mixed with seawater or different NaCl concentrations exhibited a similar cumulative heat at 72 hours.

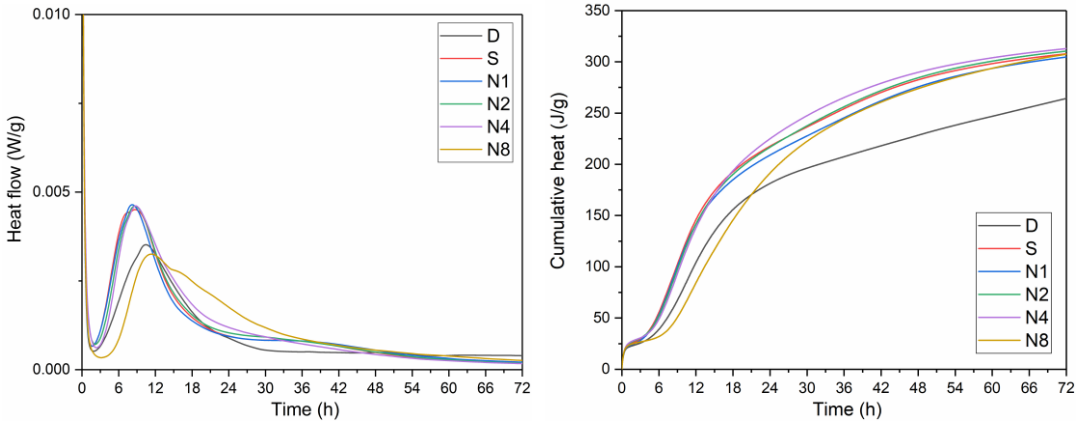

Fig. 10 Hydration heat evolution for the pastes mixed with different Na^+ ion concentrations

In addition, the evolution of hydration products was also found by XRD and Rietveld method with

increasing the mixing NaCl concentration solutions. As shown in Fig. 11, Friedel's salt, as a new product, was formed in the seawater or NaCl mixed specimens instead of hemicarboaluminate, compared with the DI water mixed specimen. Additionally, it is interesting to note that the XRD curves of N1, N2, N4 and N8 specimens at 28 d remained unchanged, indicating that the phase compositions including the types of hydration products and unhydrated clinkers did not change as Portland cement was mixed with different NaCl concentration solutions. Moreover, the contents of each phase were quantified, as listed in Table 4. It can be seen that the contents of unhydrated C_3S in the seawater or NaCl solution mixed specimens at 28 d were obviously lower than that in the DI water mixed specimen, corresponding to the acceleration hydration effect of seawater or NaCl solution, which was also consistent with the results of 72-hour cumulative heat. Furthermore, the effect of NaCl concentration on phase content at the later age was negligible, i.e., the contents of each unhydrated clinker (C_3S, C_2S, C_3A and C_4AF) and hydration product (CH and Friedel's salt) in the N1, N2, N4 and N8 specimens were nearly the same, which was also in agreement with the results of 72-hour cumulative heat. According to the results of hydration heat and XRD, the evolution of mixing NaCl concentration mainly influenced the early-age hydration rate, but did not change the later-age hydration degree and hydration products; and thus, the formed ASR gel in different specimens was the critical factor causing the different ASR expansion.

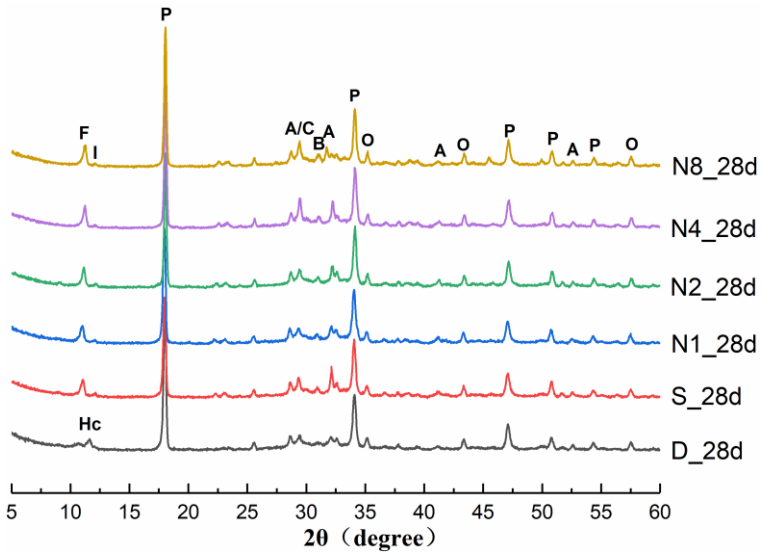

Fig. 11 XRD patterns of the pastes mixed with different Na^+ ion concentrations at 28 days. (Legend: E: ettringite (AFt); F: Friedel's salt; Hc: hemicarboaluminate; P: CH; A: C_3S; B: C_2S; I: C_4AF; C: Calcite; O: Al_2O_3)

Table 4 Quantitative XRD results of different pastes at 28 days.

Sample	C_3S	C_2S	C_3A	C_4AF	Calcite	CH	Friedel's salt	Acn	R_{wp}
D	15.0	12.5	-	3.2	5.7	22.0	-	41.6	12.9
S	11.8	11.3	-	2.8	6.6	19.0	8.5	40.0	12.5
N1	11.6	12.0	-	3.2	6.7	19.7	8.0	38.8	12.1
N2	11.7	11.8	-	3.0	7.2	19.9	8.5	37.9	12.4
N4	11.3	11.6	-	3.2	9.5	18.7	8.1	37.6	12.9
N8	11.9	11.4	-	3.2	11.1	19.1	8.4	35.0	12.7

-: not present.

3.7 Evolution of microstructure

The microstructural evolution of each specimen dominated the change of macro crack shown in Fig. 5. Fig. 12 shows the microstructure images of each specimen at 28 days, acquired by the optical microscope of nanoindentation. The used RGA with different colors in microstructure were seen by the optical microscope, corresponding to various kinds of glass. As shown in Fig. 12, all

the surface of the recycled glass aggregates in D, S and N1 specimens at 28 days was smooth and free of ASR cracks. Similarly, no ASR cracks were present in the N2 specimen, while a long crack caused by the swelling pressure of ASR gel was detected between RGA and hardened cement paste matrix. The ASR crack appeared in the interior of the glass aggregates as the mixing Na^+ ion concentration increased up to four times the sodium concentration of seawater. Moreover, ASR dramatically developed and a growing wider crack was found with mixing a larger Na^+ ion concentration.

Additionally, the microstructural evolution of specimens was further confirmed by BSE measurement, as shown in Fig. 13. The RGA and cement matrix could be clearly distinguished from BSE images. Furthermore, the ASR crack was clearly detected at the same position in Fig. 12 (i.e., in the interface between RGA and hardened cement paste matrix of N2 specimen or on the surface of RGA of N4 and N8 specimens). Therefore, the microstructural evolution observed by optical microscope images and BSE image was consistent with the macro crack (Fig. 5) and the expansion change (Fig. 3) and the strength change (Fig. 4)

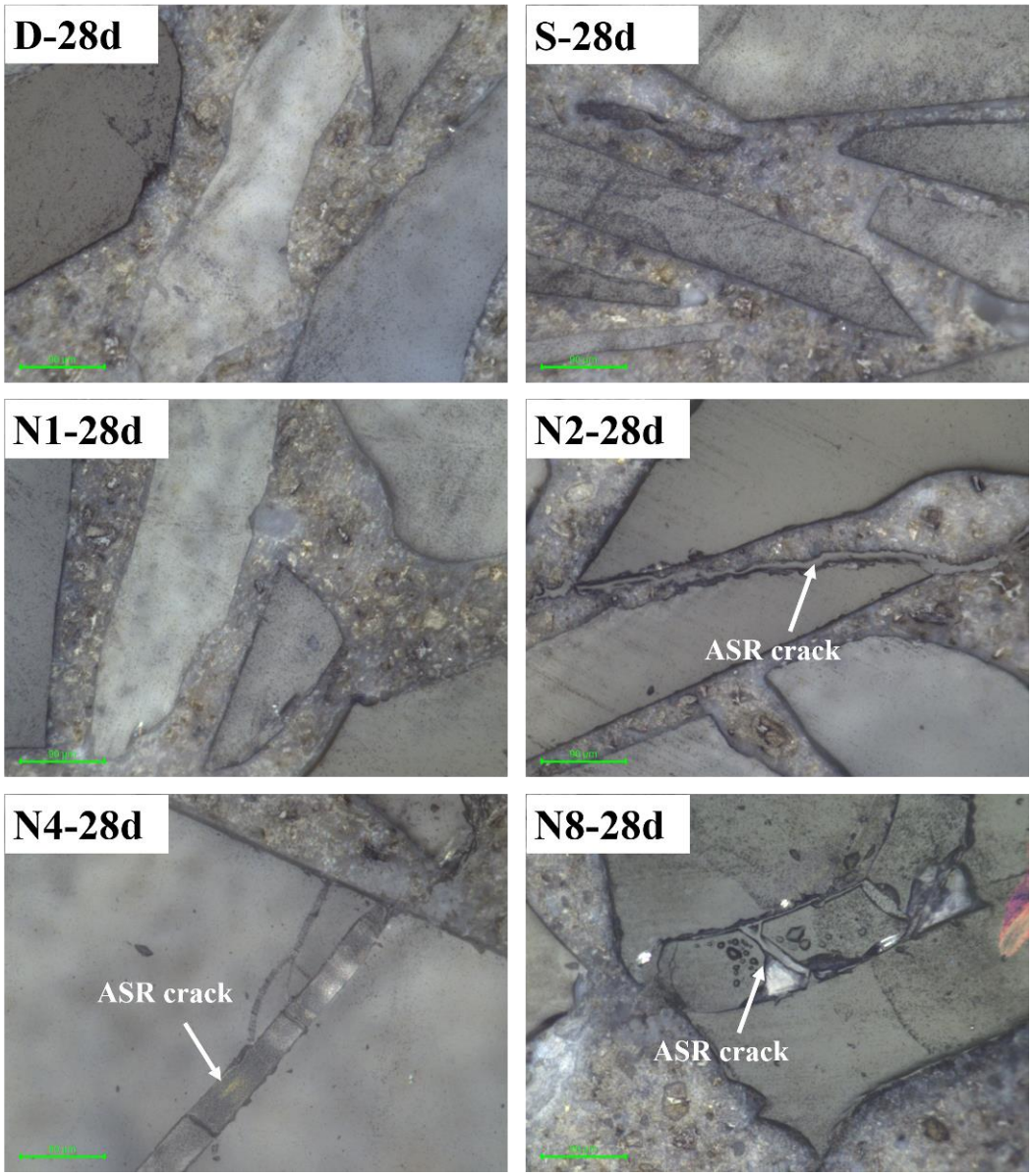

Fig. 12 Microstructure images acquired by the optical microscope of nanoindentation

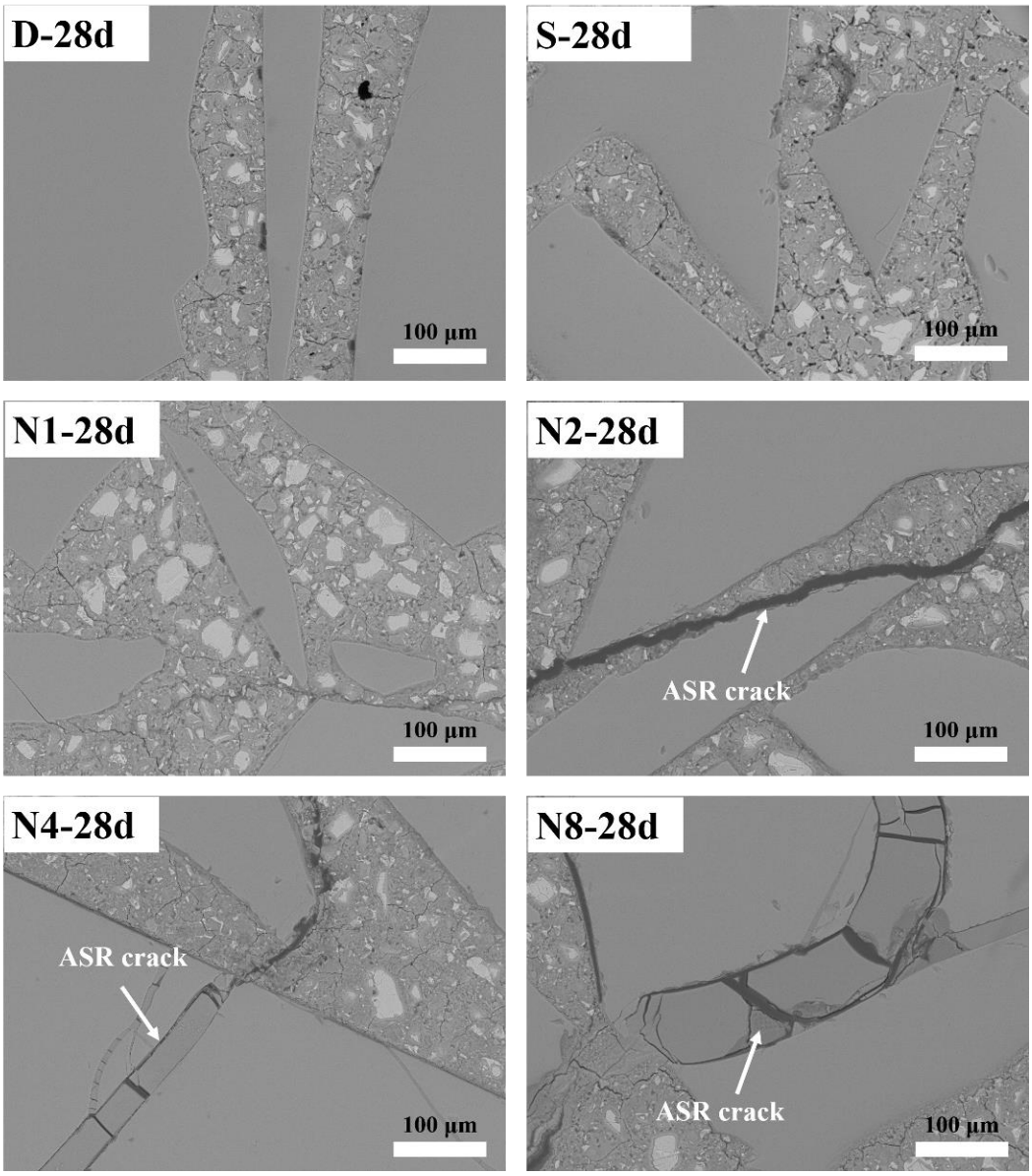

Fig. 13 BSE images of different specimens at 28 days

3.8 ASR crack process of glass aggregate characterized by nanoindentation

Generally, ACR crack was proved to exist in the case that the recycled glass cullet served as the fine aggregates in previous works. [48-51]. And yet, few studies have investigated in detail the ASR crack process of glass. In this work, nanoindentation method was used to characterize the crack process from a nanomechanical strength perspective.

Firstly, the crack process of the specimen mixed with a high Na^+ concentration and suffering from a large ASR expansion was investigated, and Fig. 14a lists the interest region of N8 specimen, which contained various destroy layers or interfaces. Regarding the nanoindentation measurements of N8 specimen, a 5 × 20 grid with 5 μm interval was chosen in this interest region. Fig. 14b shows the microstructure image after nanoindentation test, and it is interesting to find that the traces after nanoindentation remained in the white zone and the crack (or resin) zone of interest region, corresponding to a stable measurement result, which indicated that these two zones exhibited a low hardness and elastic modulus. Likewise, these traces could also be clearly found in the BSE image (Fig. 13) while these in the crack zone were not detected due to the black background. Fig. 14c shows the contour map of hardness distribution in the interest region. Different layers were easily distinguished by comparing the mean hardness and contour map of hardness, which were outlined with black dashed lines in the contour map. As shown in Fig. 14c, the original glass layer without damage, located at the top zone of interest region, showed the highest hardness with an average value of 8.04 GPa. The resin layer was also the ASR crack region which was completely destroyed and impregnated by the epoxy resin during specimen preparation. Furthermore, two partially destroyed glass layers were located between two resin layers or between the original glass layer and the resin layer, exhibiting a relatively lower hardness (about 1.91 GPa) compared with the original glass layer. At the bottom zone of interest region, the severely destroyed glass layer showed the lowest hardness with a mean value of 0.13 GPa, comparing with two other glass layers. Therefore, the glass suffering from ASR expansion exhibited the partially and severely destroyed period, along with the ASR crack zones corresponding to the completely destroyed period. Interestingly, the various layer outlines and the

dividing lines between two different layers in the contour map of hardness (Fig. 14c) were well consistent with those shown in the microstructure images (Fig. 14b and Fig. 13). Moreover, the contour map of elastic modulus in the interest region (Fig. 14d) showed the similar layer outlines compared to that of hardness (Fig. 14c), and the average elastic modulus of the original glass layer, the partially destroyed glass layer and the severely destroyed glass layer gradually decreased from 83.6 GPa to 36.4 GPa to 6.3 GPa. Therefore, the change of hardness and elastic modulus suggested different destroyed degrees of glass matrix after suffering from ASR.

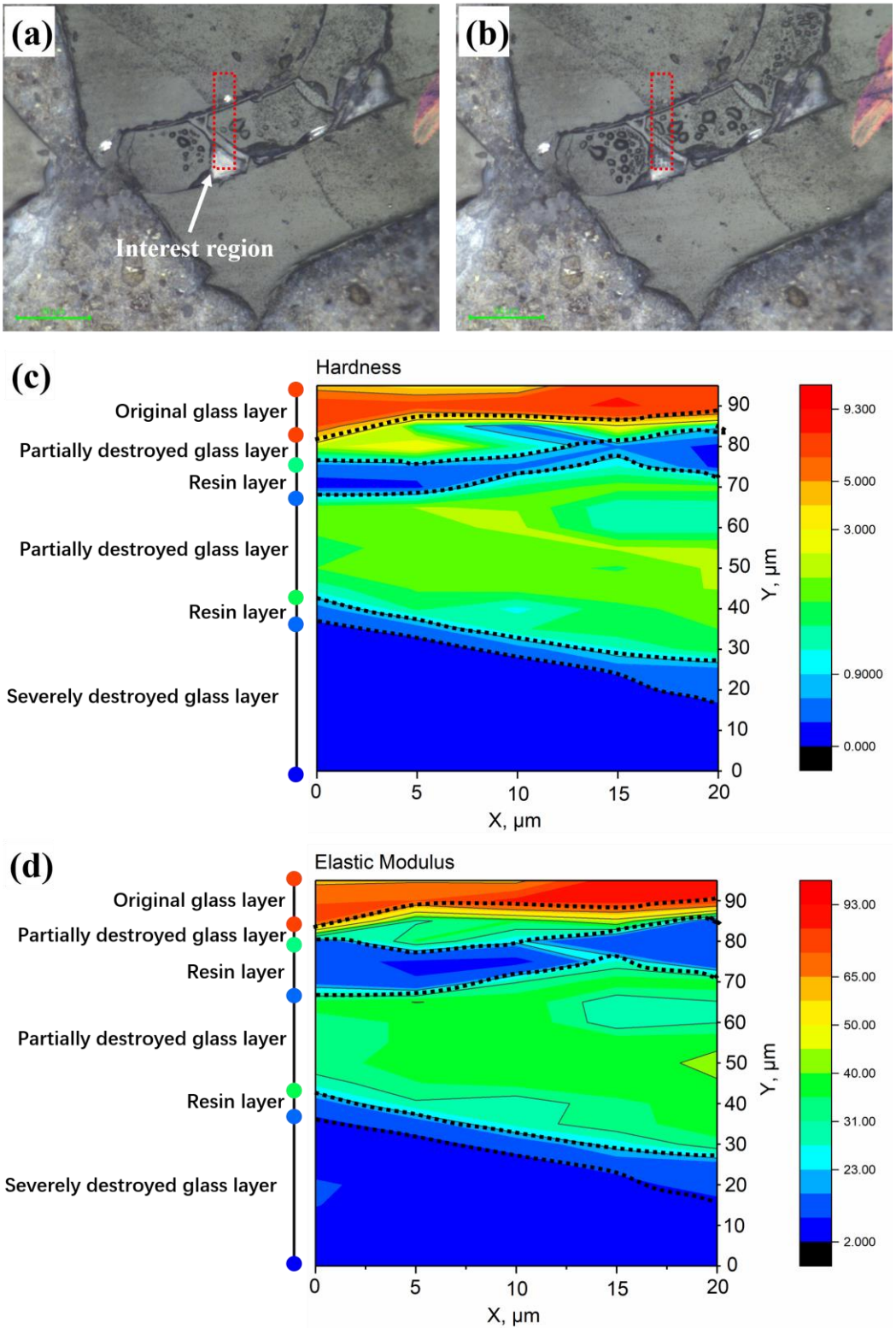

Fig. 14 ASR crack process of N8 specimen. (a) the original image without nanoindentation, (b) the microstructure image after nanoindentation, (c) the contour map of hardness distribution in the interest region, (d) the contour map of elastic modulus in the interest region

Furthermore, the chemical compositions of glass with different destroyed degrees would be changed. Fig. 15 shows the results of elemental mapping in BSE interest region of N8 specimen at 28 days. According to the mapping result of C element, the resin ($(C_{11}H_{12}O_3)_n$) layer can be easily detected (i.e., the black zones in the interest region of BSE image) since the C content in this zone was obviously higher than that in other zones where the C content was sourced from carbon coated process during BSE specimen preparation. The three other zones with the same dark gray background in the BSE images represented the glass layers with various chemical compositions. According to the mapping of Si element, the severely destroyed glass layer, shown in Fig. 15, exhibited a significantly low content of Si element compared to other glass layers. Moreover, EDS measurements were conducted to determine the content value of different elements. The average Si contents of the severely destroyed glass layer, the middle glass layer and the top glass layer were 1.2%, 19.1% and 21.9%. Therefore, the element contents of glass gradually decreased along the direction from the top to the bottom of the interest region, especially for the large element loss in the bottom zone, indicating various destroyed degrees of glass. The results of mapping and EDS were well consistent with the nanoindentation results, suggesting that the glass suffering from ASR would exhibit a decrease of hardness and elastic modulus and a content loss of Si element.

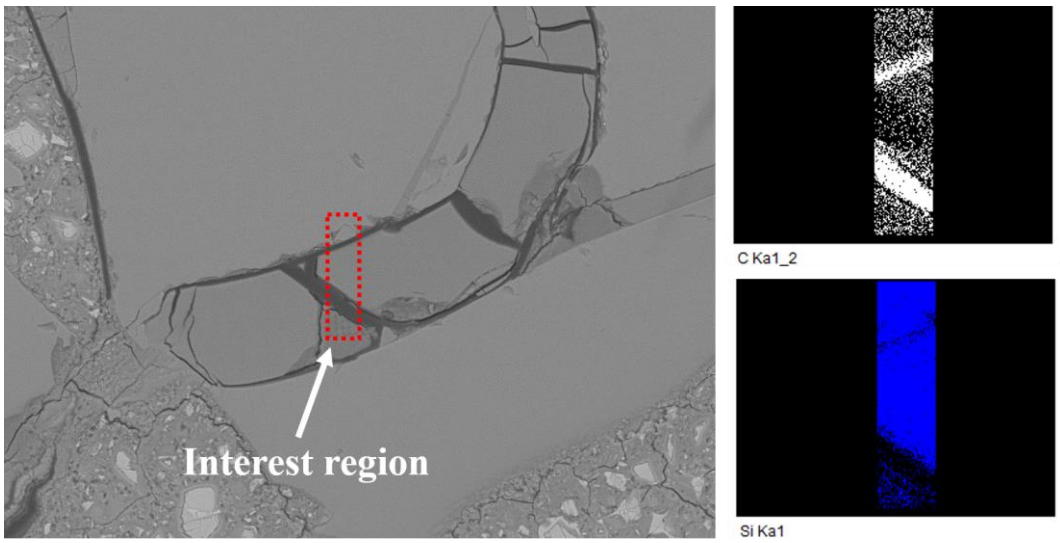

Fig. 15 Elemental mapping of the interest region in BSE image of N8 specimen at 28 days

Secondly, the crack process of the specimen mixed with a low Na^+ concentration and suffering from a slight ASR expansion was investigated, and Fig. 16a lists the interest region of N2 specimen, which contained the cement paste layer, resin layer and glass layer. A 10 × 10 grid with 5 μm interval was chosen in the interest region of N2 specimen during nanoindentation measurements. It can be seen in the contour map of hardness (Fig. 16b) that the various layer outlines were well consistent with those shown in the microstructure images (Fig. 16a and Fig. 13), and the cement paste layer exhibited an average hardness of 0.35 GPa. Likewise, the contour map of elastic modulus (Fig. 16c) showed a similar layer outline compared to that of hardness (Fig. 16b), and the cement paste layer showed its typical elastic modulus of 12.6 GPa. Interestingly, the resin layer (i.e., ASR crack zone) only existed between the cement paste layer and the glass layer instead of the internal region of glass as occurred in N8 specimen (Fig. 14), which indicated that the ASR gel formed at a low Na^+ concentration exhibited a comparatively small expansion pressure, and only induced the ASR crack in the zone between the cement paste layer and the glass layer since the cement paste layer had lower hardness and elastic modulus, and was more easily

destroyed compared with the glass layer. However, the ASR gel would have a strong expansion pressure when the specimen was mixed with a high Na^+ concentration, resulting in the ASR crack in the internal region of glass.

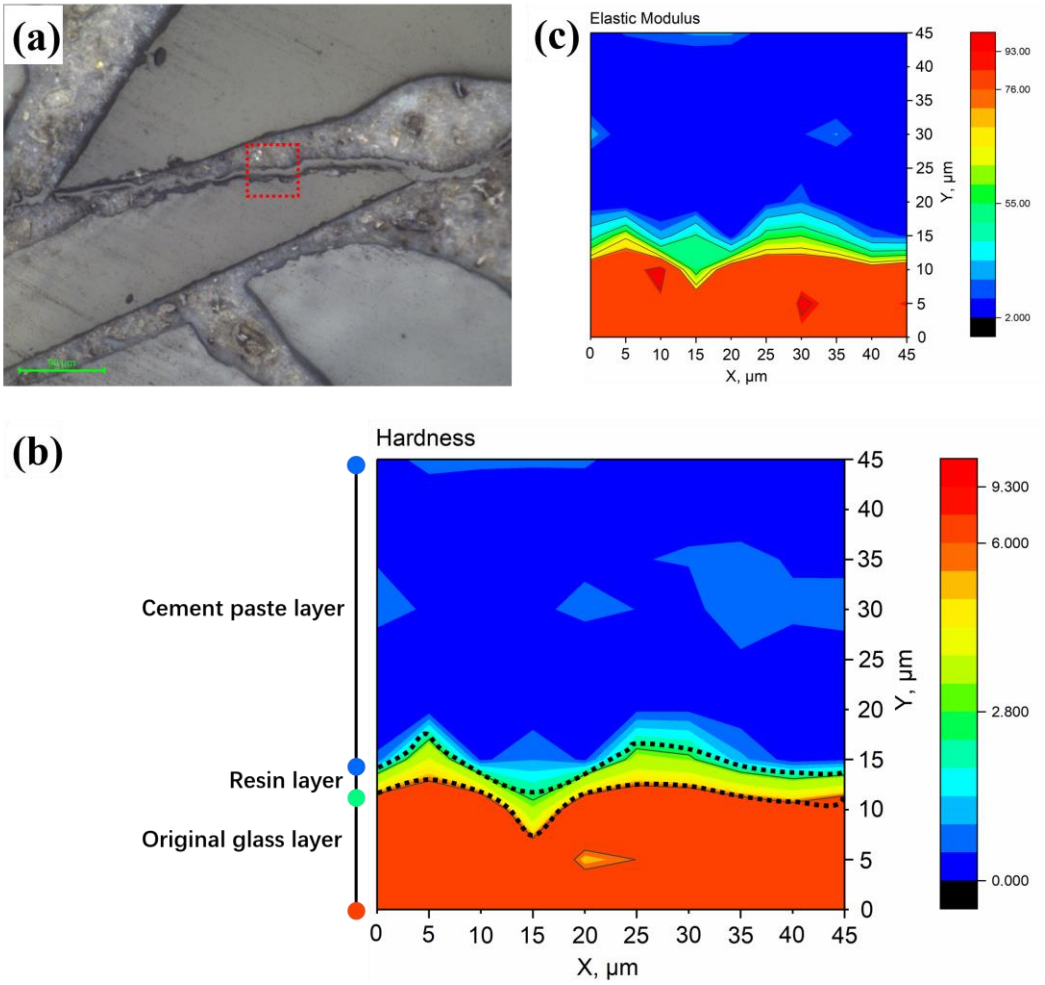

Fig. 16 ASR crack process of N2 specimen. (a) the interest region investigated in N2 specimen, (b) the contour map of hardness distribution in the interest region, (c) the contour map of elastic modulus in the interest region

In addition, various layers were also detected by the elemental mapping of BSE image, as shown in Fig. 17. The resin layer or ASR crack zone in N2 specimen was clearly found according to the high C element content. The cement paste layer exhibited a relatively lower Si content, compared

with the glass layer. Furthermore, the mapping results of N2 specimen (Fig. 17) were well consistent with the nanoindentation results (Fig. 16), and different layers could be detected based on their typical hardness, elastic modulus and chemical composition.

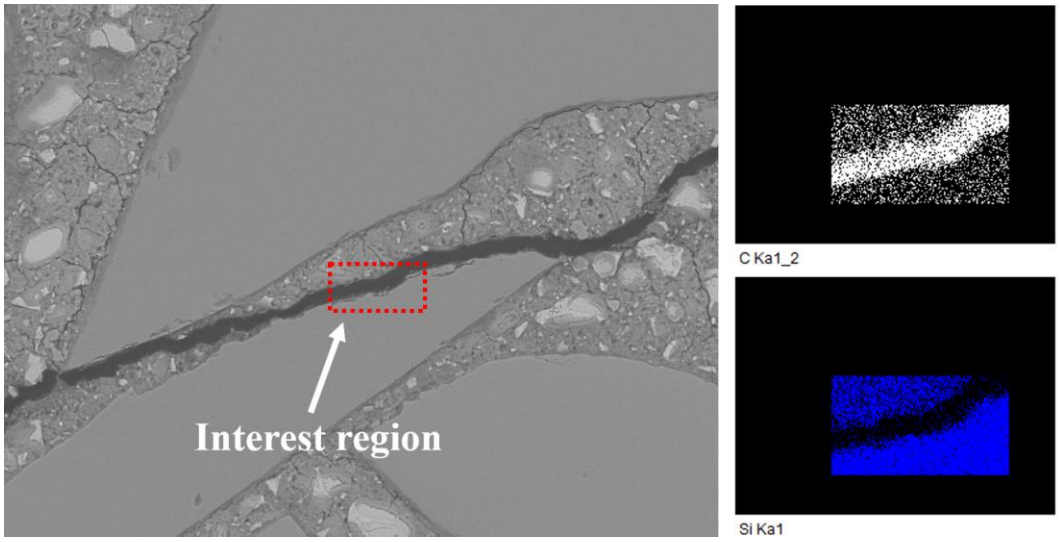

Fig. 17 Elemental mapping of the interest region in BSE image of N2 specimen at 28 days

4. Discussion

Generally, the post-consumer waste glass is an important part of municipal solid waste, whose disposal would take up valuable landfill space and waste its useful resource as well. Thus, much of research recycled the glass resource as a replacement for river sand, and the produced building materials exhibited excellent performances including drying shrinkage, water absorption, properties of fresh mortar, and resistance to chloride, acid and high temperature attack, etc. [48, 50, 52-54]. However, the addition of RGA would potentially induce ASR crack owing to the high content of amorphous silica in glass, and various improvement methods were proposed for restricting ASR occurrence in previous studies [48-50, 55].

This work provided a novel insight that the potential ASR character of RGA was used for fast investigating the effect of mixing Na^+ ion concentration on ASR of SSC, not only recycling this municipal solid waste but also giving a useful test method regarding ASR of SSC. Generally, recycled glass has a sodium oxide content of about 13%; but the sodium oxide in the glass cannot induce ASR reaction based on the fact that although the glass aggregate content is high (the aggregate-to-cement ratio was 2.25), D, S and N1 samples did not show ASR crack (Fig. 3); but with increasing the Na^+ concentration in the mixing solution up to twice the sodium concentration of seawater, ASR crack occurred (Fig. 3) although the water-to-cement ratio was only 0.47; moreover, the ASR expansion obviously increased with an increase of mixing Na^+ concentration (Fig. 3). Thus, only Na^+ ion in the mixing solution could induce ASR crack. The influence of sodium in glass on ASR crack was negligible because the sodium might be stable in glass and cannot react with the external ions, and the specific reason will be investigated in future. Furthermore, this work might also provide a perspective regarding the use of RGA as a replacement of fine aggregate of SSC in the future. In addition, the traditional ASTM C1260 method was not suitable to fast investigate the effect of mixing Na^+ ion concentration on ASR due to the very weak effect of mixing Na^+ ion compared with large numbers of external Na^+ ion added, as shown in Fig. 1. Additionally, the results of the second test method were able to discriminate the expansive behaviour of the mortars prepared with the various NaCl solutions, and were congruent with the salinity of the mixing solutions. But even prolonged the curing age up to 28 days, the expansion values of all specimens were very low, as shown in Fig. 2, and no ASR cracks were present in all specimens. Thus, 50% RGA cannot provide enough active SiO_2 for fast ASR occurrence, and it might need a long time for the second test method to assess ASR.

Thus, the test method should be modified for fast investigating the effect of mixing Na^+ ion concentration on ASR of SSC, i.e., curing in water bath at 80 °C and the usage of 100% RGA were suggested, as shown in Fig. 3. In addition, the threshold expansion value considered for the modified test methods (expansion of 0.1%) was the same of ASTM C1260. This is because that the specimens (i.e., N2, N4 and N8) showed ASR expansion cracks when the expansion values were higher than 0.1%, but the specimens (i.e., D, S and N1) did not show cracks when the expansion values were lower than 0.1%, as shown in Fig. 5. Moreover, the 28-day compressive strength of N2 specimen was obviously decreased when the expansion value of N2 specimen was higher than 0.1%; but the expansion values of S and N1 specimens were lower than 0.1% at 28 days, and S and N1 specimens had a similar 28-day compressive strength compared to D specimen and their compressive strengths were not degraded at 28 days, as shown in Fig. 4. This fast test method revealed that when mixed with twice and above the sodium concentration of seawater, the specimen would exhibit ASR expansion of 0.1% threshold (Fig. 3), dramatically decreasing strength (Fig. 4), coarsening of nanopore distribution (Fig. 7), and increasingly developed cracks (Figs. 5, 12 and 13). Also, the ASR crack would firstly occur between the cement paste layer and the glass layer (Fig. 16), and then developed in the internal zone of RGA (Fig. 14). However, the composition and content of hydration products were not obviously different (Table 4). In addition, the specimens mixed with seawater or the same sodium concentration as the seawater showed the almost similar expansion curves (Fig. 3), indicating that the NaCl solution could be used as a replacement of seawater for assessing ASR of SSC. Also, those two specimens did not show ASR crack at 28 days of curing age, but the expansions lower than 0.1% could not necessarily

correspond to non-reactive mortars due to possible alkali leaching, i.e., the low levels of expansion and the absence of ASR signs observed for N1 and S specimens subjected to the third test method could be ascribed to a reduction of the alkali level of mortars below the reactivity threshold of RGA. But these alkali ions would still react with RGA although the alkali ions with a limited amount were leached and entered into the external curing water, the ASR expansion could still occur at long-term ages if present, and thus a long-term test needs to be investigated in future research.

5. Conclusion

The present work provided a novel test method for fast investigating the effect of mixing Na^+ ion concentration on ASR of SSC, i.e., using the 100% recycled glass aggregate as active aggregate and the modified ASTM C1240 method using water bath of 80 °C. The main conclusions drawn in this work are summarized as follows:

1. The ASR expansion would exceed the 0.1% ASTM C1260 threshold when the specimen was mixed with twice and above the Na^+ concentration of seawater, and the ASR expansion dramatically increased with an increase of mixing Na^+ concentration. Correspondingly, the compressive strength significantly decreased at a high mixing Na^+ concentration. In addition, ASR of SSC could be assessed using NaCl solution as a replacement of seawater, and the expansion of specimens mixed with seawater or the same sodium concentration as the seawater was below the threshold value within 28 days of curing age.

2. No ASR cracks on the macro and micro level were detected in the specimens mixed with seawater or the same sodium concentration as the seawater. With mixing with twice and above the sodium concentration of seawater, the specimens exhibited an increasingly severe macro ASR crack ranging from 33.8 um to 263.6 um to 513.1 um, and a micro ASR crack in the interface between RGA and hardened cement paste matrix or in the interior region of RGA. Additionally, the mix of NaCl solution would coarsen nanopore distribution.

3. An extremely high mixing NaCl concentration would delay the hydration rate at the very early age, but exhibited a similar cumulative heat at 72 hours of hydration compared to seawater or the NaCl solution with other concentrations. Moreover, the specimen mixed with seawater or NaCl solution with different concentrations almost exhibited the same later-age hydration degree, product compositions and product content.

4. The ASR crack process of RGA was further investigated from a nanomechanical strength perspective using nanoindentation method. Regarding the specimen suffering from a severe ASR expansion, the glass matrix would be destroyed, including the original glass layer, the partially destroyed glass layer and the severely destroyed glass layer. In addition, the glass matrix exhibited different hardness, elastic modulus, and Si contents based on the destroyed degree. Regarding the specimen suffering from a slight ASR expansion, the ASR crack was only induced in the interface between the cement paste layer and the glass layer.

Acknowledgments

We wish to thank the financial supports of National Natural Science Foundation of China (52108252), the Theme-Based Research Scheme of the Research Grants Council of the Hong Kong SAR Government (T22-502/18-R), Science and Technology Project of Hebei Education Department (BJK2023023), Natural Science Foundation of Hebei Province (E2021203147). The project is also supported by Key Laboratory of Advanced Civil Engineering Materials (Tongji University), Ministry of Education (No. 202305).

References

[1] S.A. Miller, A. Horvath, P.J.M. Monteiro, Impacts of booming concrete production on water resources worldwide, Nat. Sustain. 1 (2018) 69-76.

[2] T. Nishida, N. Otsuki, H. Ohara, et al. Some considerations for applicability of seawater as mixing water in concrete, J. Mater. Civ. Eng. 27 (7) (2015). B4014004-1-7.

[3] O. Bozorg-Haddad, B. Zolghadr-Asli, P. Sarzaeim, M. Aboutalebi, X. Chu, H. A. Lo´aiciga, Evaluation of water shortage crisis in the Middle East and possible remedies, J. Water Supply Res. Technol. AQUA 69 (1) (2020) 85-98.

[4] Y. Sun, J. Lu, C.S. Poon, Strength degradation of seawater-mixed alite pastes: an explanation from statistical nanoindentation perspective, Cem. Concr. Res. 152 (2022) 106669.

[5] J. Xiao, C. Qiang, A. Nanni, K. Zhang, Use of sea-sand and seawater in concrete construction: Current status and future opportunities, Constr. Build. Mater. 155 (2017) 1101-1111.

[6] U. Ebead, D. Lau, F. Lollini, A. Nanni, P. Suraneni, T. Yu, A review of recent advances in the science and technology of seawater-mixed concrete, Cem. Concr. Res. 152 (2022) 106666.

[7] Y. Zhao, X. Hu, C. Shi, Z. Zhang, D. Zhu, A review on seawater sea-sand concrete: Mixture proportion, hydration, microstructure and properties, Constr. Build. Mater. 295 (2021) 123602.

[8] P. Li, W. Li, Z. Sun, L. Shen, D. Sheng, Development of sustainable concrete incorporating seawater: A critical review on cement hydration, microstructure and mechanical strength, Cem. Concr. Compos. 121 (2021) 104100.

[9] A. Ahmed, S. Guo, Z. Zhang, C. Shi, D. Zhu, A review on durability of fiber reinforced polymer (FRP) bars reinforced seawater sea sand concrete, Constr. Build. Mater. 256 (2020) 119484.

[10] T. Dhondy, A. Remennikov, M.N. Shiekh, Benefits of using sea sand and seawater in concrete: a comprehensive review, Aust. J. Struct. Eng. 20 (4) (2019) 280-289.

[11] M. Guo, B. Hu, F. Xing, et al., Characterization of the mechanical properties of eco-friendly concrete made with untreated sea sand and seawater based on statistical analysis, Constr. Build. Mater. 234 (2020) 117339.

[12] Z. Wang, X. Zhao, G. Xian, et al., Long-term durability of basalt- and glass-fiber reinforced polymer (BFRP/GFRP) bars in seawater and sea sand concrete environment, Constr. Build. Mater. 139 (2017) 467-489.

[13] J. Teng, Y. Xiang, T. Yu, Z. Fang, Development and mechanical behaviour of ultra-high-performance seawater sea-sand concrete, Adv. Struct. Eng. 22 (14) (2019) 3100-3120.

[14] Z. Dong, Y. Sun, H. Zhu, G. Wu, Z. Yan, F. Lu, Behavior and modeling of seawater sea-sand coral aggregate concrete-filled BFRP tubular columns under eccentric compression, Compos. Struct. 288 (2022) 115392.

[15] S. Han, A. Zhou, J. Ou, Relationships between interfacial behavior and flexural performance of hybrid steel-FRP composite bars reinforced seawater sea-sand concrete beams, Compos. Struct. 277 (2021) 114672.

[16] Z. Lu, Y. Li, J. Xie, Durability of BFRP bars wrapped in seawater sea sand concrete, Compos. Struct. 255 (2021) 112935.

[17] Y. Zhang, Y. Wei, J. Bai, G. Wu, Z. Dong, A novel seawater and sea sand concrete filled FRP-carbon steel composite tube column: Concept and behaviour, Compos. Struct. 246 (2020) 112421.

[18] Y. Zhang, Y. Sun, H. Zheng, Y. Cai, W.L. Lam, C.S. Poon, Mechanism of strength evolution of seawater OPC pastes, Adv. Struct. Eng. 24 (6) (2021) 1256-1266.

[19] P. Li, W. Li, T. Yu, F. Qu, V.W.Y. Tam, Investigation on early-age hydration, mechanical properties and microstructure of seawater sea sand cement mortar, Constr. Build. Mater. 249 (2020) 118776.

[20] Y. Sun, Y. Zhang, Y. Cai, et al., Mechanisms on Accelerating Hydration of Alite Mixed with Inorganic Salts in Seawater and Characteristics of Hydration Products, Acs Sustain Chem Eng. 9 (31) (2021) 10479-10490.

[21] S.K. Kaushik, S. Islam, Suitability of sea water for mixing structural concrete exposed to a marine environment, Cem. Concr. Compos. 17 (3) (1995) 177-185.

[22] A. Younis, U. Ebead, P. Suraneni, A. Nanni, Fresh and hardened properties of seawater-mixed concrete, Constr. Build. Mater. 190 (2018) 276-286.

[23] C.G. Girish, D. Tensing, K.L. Priya, Dredged offshore sand as a replacement for fine aggregate in concrete, Int. J. Eng. Sci. Emerg. Technol. 8 (3) (2015) 88-95.

[24] M.M. Islam, M.S. Islam, M. Al-Amin, M.M. Islam, Suitability of sea water on curing and compressive strength of structural concrete, J. Civ. Eng. (the Institution of Engineers, Bangladesh) 40 (1) (2012) 37-45.

[25] F.M. Wegian, Effect of seawater for mixing and curing on structural concrete, IES J. Part A Civil Struct. Eng. 3 (4) (2010) 235–243.

[26] S.A. Yaseen, G.A. Yiseen, C.S. Poon, Z. Li, Influence of seawater on the morphological evolution and the microchemistry of hydration products of tricalcium silicates (C_3S). Acs Sustain. Chem. Eng. 8 (2020) 15875-15887.

[27] L. Montanari, P. Suraneni, M. Tsui-Chang, et al., Hydration, pore solution, and porosity of cementitious pastes made with seawater. J. Mater. Civ. Eng. 31(8) (2019) 04019154.

[28] Y. Cai, D. Xuan, P. Hou, J. Shi, C.S. Poon, Effect of seawater as mixing water on the hydration behaviour of tricalcium aluminate, Cem. Concr. Res. 149 (2021) 106565.

[29] Q. Li, H. Geng, Z. Shui, Y. Huang, Effect of metakaolin addition and seawater mixing on the properties and hydration of concrete, Appl. Clay Sci. 115 (2015) 51-60.

[30] K. De Weerdt, A. Colombo, L. Coppola, H. Justnes, M.R. Geiker, Impact of the associated cation on chloride binding of Portland cement paste, Cem. Concr. Res. 68 (2015) 196-202.

[31] K. De Weerdt, D. Orsáková, M.R. Geiker, The impact of sulphate and magnesium on chloride

binding in Portland cement paste, Cem. Concr. Res. 65 (2014) 30-40.
[32] A.G. Modupeola, F.A. Olutoge, The effect of seawater on shrinkage properties of concrete, Int. J. Res. Eng. Technol. 2 (10) (2014) 1-12.
[33] M. Khatibmasjedi, S. Ramanathan, P. Suraneni, A. Nanni, Shrinkage behavior of cementitious mortars mixed with seawater, Adv. Civil Eng. Mater. 8 (2) (2019) 64-78.
[34] A. Adiwijaya, H. Hamada, Y. Sagawa, D. Yamamoto, Expansion characteristics of seawater mixed concrete due to alkali-silica reaction, in: 40th Conference on Our World in Concrete & Structures, Singapore, 2015.
[35] A. Adiwijaya, H. Hamada, Evaluation of seawater-mixed concrete from the viewpoint of strength and durability, in: Proceedings of International Symposium on Concrete Technology, Makassar, Indonesia, 2017.
[36] S. Khatibmasjedi, F.J. De Caso y Basalo, A. Nanni, SEACON: redefining sustainable concrete, in: Fourth International Conference on Sustainable Construction Materials and Technologies, Las Vegas, NV, USA (2016, August).
[37] K. De Weerdt, B. Lothenbach, M.R. Geiker, Comparing chloride ingress from seawater and NaCl solution in Portland cement mortar, Cem. Concr. Res. 115 (2019) 80-89.
[38] ASTM D1141–98, Standard Practice for the Preparation of Substitute Ocean Water, ASTM International, West Conshohocken, PA, USA, 2013, p. 2013.
[39] Y. Zhang, Q. Zhao, Z. Gao, J. Chang, Nanostructural evolution of $Al(OH)_3$ gel formed by the cubic and orthorhombic ye'elimite clinkers of calcium sulfoaluminate cements in an ultra-wide hydration temperature range, Cem. Concr. Res. 150 (2021) 106607.
[40] T. Zhang, T. Li, Z. Zhou, M. Li, Y. Jia, C. Cheeseman, A novel magnesium hydroxide sulfate hydrate whisker-reinforced magnesium silicate hydrate composites, Compos B Eng 198 (2020) 108203.
[41] B. Zhan, D. Xuan, C.S. Poon, Enhancement of recycled aggregate properties by accelerated CO_2 curing coupled with limewater soaking process, Cem. Concr. Compos. 89 (2018) 230-237.
[42] W. Ashraf, N. Tian, Nanoindentation assisted investigation on the viscoelastic behavior of carbonated cementitious matrix: Influence of loading function, Constr. Build. Mater. 127 (2016) 904-917.
[43] W. Ashraf, J. Olek, J. Jain, Microscopic features of non-hydraulic calcium silicate cement paste and mortar, Cem. Concr. Res. 100 (2017) 361-372.
[44] P.K. Mehta, P.J.M. Monteiro, Concrete: Microstructure, Properties, and Materials, McGraw-Hill Publishing, London, (2006).
[45] H. Alanazi, J. Hu, Y. Kim, Effect of slag, silica fume, and metakaolin on properties and performance of alkali-activated fly ash cured at ambient temperature, Constr. Build. Mater. 197 (2019) 747-756.
[46] D. Ravikumar, N. Neithalath, An electrical impedance investigation into the chloride ion transport resistance of alkali silicate powder activated slag concretes, Cem. Concr. Compos. 44 (2013) 58-68.
[47] G.C. Edwards, R.L. Angstadt, The effect of some soluble inorganic admixtures on the early hydration of portland cement, J. Appl. Chem. 16 (5) (1966) 166-168.
[48] P. He, B. Zhang, J. Lu, C.S. Poon, ASR expansion of alkali-activated cement glass aggregate mortars, Constr. Build. Mater. 261 (2020) 119925.
[49] Y. Cai, D. Xuan, C.S. Poon, Effects of nano-SiO2 and glass powder on mitigating alkali-silica

reaction of cement glass mortars, Constr. Build. Mater. 201 (2019) 295-302.
[50] S. Yang, C.S. Poon, T.C. Ling, Distribution of ASR gel in conventional wet-mix glass mortars and mechanically produced dry-mix glass blocks, Constr. Build. Mater. 229 (2019) 116916.
[51] S. Yang, H. Cui, C.S. Poon, Assessment of in-situ alkali-silica reaction (ASR) development of glass aggregate concrete prepared with dry-mix and conventional wet-mix methods by X-ray computed micro-tomography, Cem. Concr. Compos. 90 (2018) 266-276.
[52] K.H. Tan, H. Du, Use of waste glass as sand in mortar: Part I − Fresh, mechanical and durability properties, Cem. Concr. Compos. 35 (1) (2013) 109-117.
[53] T. Ling, C. Poon, S. Kou, Feasibility of using recycled glass in architectural cement mortars, Cem. Concr. Compos. 33 (8) (2011) 848-854.
[54] M. Guo, Z. Chen, T. Ling, C.S. Poon, Effects of recycled glass on properties of architectural mortar before and after exposure to elevated temperatures, J. Clean. Prod. 101 (2015) 158-164.
[55] M. Thomas, The effect of supplementary cementing materials on alkali-silica reaction: A review, Cem. Concr. Res. 41 (12) (2011) 1224-1231.